

¹ The imbricated foreshock and aftershock activities of
² the Balsorano (Italy) M_w 4.4 normal fault earthquake
³ and implications for earthquake initiation

⁴ H. S. Sánchez-Reyes¹, D. Essing¹, E. Beaucé², P. Poli¹¹

⁵ *¹Institute of Earth Sciences, University Grenoble Alpes, Grenoble 38100, France*

⁶ *²Department of Earth, Atmospheric, and Planetary Sciences, Massachusetts Institute of
7 Technology, Cambridge, MA, United States*

⁸ **Corresponding author: hugo.sanchez-reyes@univ-grenoble-alpes.fr*

9 **Key words:**

10 • earthquake initiation process

11 • earthquake sequence

12 • spatio-temporal evolution

13 **Key points:**

14 • The analysis of the 2019 Balsorano earthquake sequence reveals that imbricated com-
15 plex processes occur before and after the main earthquake

16 • Clear differences between foreshocks and aftershocks are highlighted by the distinct
17 spatio-temporal patterns unraveled by our analysis

18 • These results deThe results of the spatio-temporal evolution for the identified clusters
19 suggest complex evolution of the seismicity. Two fault planes are activated during
20 the sequence, with foreshocks primarily occurring on the antithetic fault plane (Fig.
21 5a, cross-section), similarly to part of the foreshock activity that was observed for
22 the L'Aquila normal fault earthquake ([Chiaraluce et al., 2011](#)). Relying only on our
23 observations, it is hard to unravel which mechanism(s) might be responsible for the
24 occurrence of the foreshocks, and thus the driving of the main event. For example,
25 there are no exponential or power-law increments of events seen while approaching
26 the main event ([Papazachos, 1975](#); [Kagan and Knopoff, 1978](#)), which might suggest
27 accelerating aseismic slip ([Dodge et al., 1996](#); [Bouchon et al., 2011](#); [Tape et al., 2018](#)).
28 Neither are any spatial patterns seen (*e.g.*, migrations) that might suggest the same
29 mechanism, or might alternatively indicate triggering by stress transfer ([Dodge et al.,
30 1996](#); [Ellsworth and Bulut, 2018](#); [Yoon et al., 2019](#)). However, we clearly outline the
31 differences between the foreshocks and aftershocks. In particular, the foreshocks occur

32 in a more temporal clustered manner, and they are closer to the hypocenter of the
33 main event (Fig. 4a). The compact and highly temporal clustered seismicity indicates
34 strong event interactions, and favors stress transfer as the mechanism for foreshock
35 occurrence (COV, [Schoenball and Ellsworth, 2017](#)). monstrate that simple earthquake
36 preparation models are not suitable enough to correctly mimic the observed complex
37 reality

Abstract

39 Foreshocks in the form of microseismicity are among the most powerful tools to
40 study the physical processes that occur before main earthquakes. However, their
41 detection and precise characterization is still sparse, especially for relatively small
42 earthquakes ($M_w < 5$). We present here a detailed foreshock analysis for the November
43 7, 2019, Balsorano (Italy) normal fault earthquake ($M_w 4.4$). To improve the
44 detection of the microseismicity before and after the mainshock, we use six three-
45 component broadband receivers at distances of less than 75 km from the targeted
46 seismicity, through template matching. To improve the understanding of the physical
47 mechanism(s) behind the earthquake initiation process, as well as other accompanying
48 phenomena, we also detail the spatio-temporal evolution of the sequence associated to
49 this medium-sized earthquake, using waveform clustering and hypocenter relocation.
50 Clear differences between foreshocks and aftershocks are revealed by this analysis.
51 Moreover, five distinct spatio-temporal patterns associated to the different seismic
52 activities are revealed. The observed spatio-temporal behavior shown by the fore-
53 shocks highlights a complex initiation process, which apparently starts on an adjacent
54 unmapped antithetic fault. Finally, the aftershock activity comprises four different
55 clusters with distinct spatio-temporal patterns, which suggests that each cluster in
56 this sequence has a distinct triggering mechanism.

57 Introduction

58 The detection of signals that can inform us about a forthcoming earthquake is fundamental
59 to build physical models that mimic the processes behind the triggering and nucleation of
60 earthquakes. These physical models are important because they provide us the basis to
61 characterize earthquakes. Therefore, the study and analysis of precursory signals are of
62 great importance. Over the last 25 years, numerous studies have reported a wide range of
63 observations that appear to be connected with the physics that precedes large seismic events

64 (e.g. Rikitake, 1975; Jones and Molnar, 1979; Molchanov et al., 1998; Eftaxias et al., 2000;
65 Virk and Walia, 2001; Singh et al., 2010; De Santis et al., 2019; Jones, 1985; Abercrombie
66 and Mori, 1996; Felzer et al., 2004; Dodge et al., 1996; Ellsworth and Bulut, 2018; Yoon
67 et al., 2019; Reasenberg, 1999; Ruiz et al., 2017, 2014a). Among these, some of the most
68 compelling are the ones based on seismological characterization of foreshock sequences,
69 as well as other seismological observations and their relationships with mainshocks (e.g.
70 Jones, 1985; Abercrombie and Mori, 1996; Reasenberg, 1999; Felzer et al., 2004; Dodge
71 et al., 1996; Bouchon et al., 2011; Ruiz et al., 2014b, 2017; Ellsworth and Bulut, 2018; Yoon
72 et al., 2019). Foreshocks are thus one of the most useful tools to understand the physics of
73 earthquake initiation in real faults (Brune, 1979; Abercrombie and Mori, 1996; Malin et al.,
74 2018). Therefore, it is important to improve foreshock observations and characterization,
75 particularly for more frequent medium-sized events (*i.e.* $M_w < 6$), as these might share
76 similar physical processes with larger events. These improved observations may shed light
77 on the physical processes that occur during the triggering and nucleation of earthquakes
78 and will drive future research that focuses on theoretical and numerical models to better
79 characterize earthquake occurrence in real and complex faults.

80 Earthquake initiation (e.g. Kato et al., 2012; Schurr et al., 2014; Tramutoli et al., 2015)
81 and earthquake nucleation/triggering (e.g. Dieterich, 1992; Ellsworth and Beroza, 1995;
82 Rubin and Ampuero, 2005) are two different, and perhaps overlapping, phases of the seis-
83 mic cycle. While the first is understood to occur over the longer term preceding a large
84 event (*i.e.*, days or months, to years), the second occurs some minutes toThe results of
85 the spatio-temporal evolution for the identified clusters suggest complex evolution of the
86 seismicity. Two fault planes are activated during the sequence, with foreshocks primarily
87 occurring on the antithetic fault plane (Fig. 5a, cross-section), similarly to part of the
88 foreshock activity that was observed for the L'Aquila normal fault earthquake (Chiaraluce
89 et al., 2011). Relying only on our observations, it is hard to unravel which mechanism(s)
90 might be responsible for the occurrence of the foreshocks, and thus the driving of the

main event. For example, there are no exponential or power-law increments of events seen while approaching the main event (Papazachos, 1975; Kagan and Knopoff, 1978), which might suggest accelerating aseismic slip (Dodge et al., 1996; Bouchon et al., 2011; Tape et al., 2018). Neither are any spatial patterns seen (*e.g.*, migrations) that might suggest the same mechanism, or might alternatively indicate triggering by stress transfer (Dodge et al., 1996; Ellsworth and Bulut, 2018; Yoon et al., 2019). However, we clearly outline the differences between the foreshocks and aftershocks. In particular, the foreshocks occur in a more temporal clustered manner, and they are closer to the hypocenter of the main event (Fig. 4a). The compact and highly temporal clustered seismicity indicates strong event interactions, and favors stress transfer as the mechanism for foreshock occurrence (COV, Schoenball and Ellsworth, 2017). seconds before the main event. Both phases, however, can be explained under the Dieterich model (1994), which relates the seismicity rate to the stressing history through a rate-and-state constitutive law. For earthquake initiation in particular for real faults, two main hypotheses are currently used to explain this process. Some authors argue that a mainshock is a consequence of a cascade process, with stress transfer in-between events, which eventually trigger the large event (*e.g.*, Dodge et al., 1996; Ellsworth and Bulut, 2018; Yoon et al., 2019). Alternatively, the initiation of an earthquake can be understood as an aseismic process that weakens the pre-existing asperities, until a larger rupture is promoted (Dodge et al., 1996; Bouchon et al., 2011; Tape et al., 2018). In the latter case, foreshocks result from the activation of brittle asperities by the surrounding slip processes. However, intermediate models that involve both triggering and aseismic slip are likely for complex faults (*e.g.* McLaskey, 2019). This complexity might result from fault heterogeneity (*e.g.*, variable stress, frictional properties) and promote imbricated sequences of foreshocks and aseismic slip (*e.g.*, Dublanchet, 2018).

The monitoring of foreshocks is today routine in laboratory experiments (Zang et al., 1998; Goebel et al., 2012; Renard et al., 2019, and references therein), while studies that focus on large earthquakes remain relatively sparse (*i.e.*, $M_w > 6$) (*e.g.*, Mogi, 1963; Aber-

118 crombie and Mori, 1996; Kato et al., 2012; Chen and Shearer, 2013; Bouchon et al., 2013;
119 Ruiz et al., 2014b). However, the recent improvements to seismological monitoring systems
120 around active faults have now provided detailed analysis of foreshocks that precede the
121 more frequent small-magnitude earthquakes ($M_w < 6$) (e.g., Savage et al., 2017; McMahon
122 et al., 2017; Malin et al., 2018). One intriguing feature that has emerged from these more
123 recent studies is the increased complexity (*i.e.*, fault interactions, volumetric processes)
124 that have been revealed through the availability of better data (e.g., near-fault receivers)
125 and more advanced detection methods (e.g., template matching) to study foreshocks. This
126 complexity might challenge the actual laboratory scale and theoretical models, which treat
127 earthquake initiation as simple physical processes that occur in smooth fault planes (Di-
128 eterich, 1992; Marone, 1998; Rubin and Ampuero, 2005; Liu and Rice, 2005). The necessity
129 for high-resolution characterization of foreshocks based on good data and advanced data
130 processing techniques was also suggested by a meta-analysis carried out by Mignan (2014),
131 which indicated resolution-dependent bias for earthquake initiation models that were re-
132 solved using seismological data.

133 To shed new light on the physical processes that occur before relatively small earth-
134 quakes, we study here the medium-sized (M_w 4.4) Balsorano normal fault earthquake and
135 its foreshock-aftershock sequence (Fig. 1). The Italian National Institute of Geophysics and
136 Volcanology (*Istituto Nazionale di Geofisica e Vulcanologia*; INGV; [online catalog](#)) reported
137 that the main event of this sequence occurred on November 7, 2019 (17:35:21.18 UTC), ap-
138 proximately 4 km southeast of Balsorano city in central Italy (Fig. 1). The hypocenter
139 of this main event was located relatively deep in the crust (14 km), close to the transi-
140 tion zone between the upper and lower crust (10-20 km in depth), where the brittle locked
141 fault transitions into the ductile regime zone (Doglioni et al., 2011). Below this depth, the
142 lower crust is relatively seismically silent (Doglioni et al., 2011). According to a geological
143 study of the location of the main event and its focal mechanism (Supplementary Material
144 Table S1), this event ruptured the Liri fault (Roberts and Michetti, 2004), which is one of

145 the major active normal faults mapped in this region. This structure accommodates the
146 low extension rate observed in this region (*i.e.*, a few millimeters per year) (Hunstad and
147 England, 1999; Westaway, 1992; D'agostino et al., 2001; Roberts and Michetti, 2004).

148 [Figure 1]

149 In addition to the mainshock of November 7, 2019, 135 events occurred close to the
150 epicenter of the main event from October 22 to November 15, 2019 (which included 25
151 foreshocks). Starting from these cataloged events, we study here the 'anatomy' of the
152 foreshocks and aftershocks, and their relationships with the main event. With this aim,
153 continuous data from six three-component stations at less than 75 km from the mainshock
154 epicenter are used (Fig. 1; Supplementary Materials Table S2). The continuous waveforms
155 recorded are analyzed using template matching techniques (Gibbons and Ringdal, 2006;
156 Shelly et al., 2007) to detect smaller events and thus to expand upon the available seismic
157 catalog. The detected events are then relocated using the double-difference method (Wald-
158 hauser, 2001), to reveal the geometry of the main fault and to obtain new insights into
159 the fault-slip behavior(s) before and after the main seismic event. Furthermore, through
160 waveform clustering, we isolate families of earthquakes that are representative of different
161 physical processes that occur in the pre- and post-mainshock period. This combination of
162 detection, relocation, and waveform clustering reveals an imbricated seismic sequence where
163 several faults were activated, and with clear differences in the spatio-temporal properties
164 of the foreshocks and aftershocks.

165 **Methods**

166 **Template matching:** The analysis starts by extending the INGV seismic catalog using the
167 template matching approach (Gibbons and Ringdal, 2006). From the 135 events reported
168 by the INGV online catalog , where 25 events are identified as foreshocks, we retain only

169 the events with available P-wave and S-wave picks for all of the six stations used. We then
170 extract 4 s of signal, starting 1 s before the phase arrival time from the band-pass filtered
171 data (5-20 Hz). Using the pre-picked signals, we estimate the signal-to-noise ratio and
172 retain as templates only those events with a signal-to-noise ratio >3 at all of the stations.
173 With this data selection, 23 events are obtained (including three foreshocks) that are the
174 templates used for scanning the continuous data (Supplementary Materials Table S4). We
175 use three-component data with P waves extracted from the vertical component, and S waves
176 extracted from the East and North components.

177 In all, 28 days of continuous data are processed, from October 22 (*i.e.*, 16 days before
178 the mainshock) to November 15, 2019, using the fast matched filter algorithm from [Beaucé
et al. \(2017\)](#). The detection thresholds are set to 12 times the daily median absolute devi-
179 ation of the summed correlation coefficients over the array of stations. Finally, consecutive
180 detections with differential times of <3 s are removed (*i.e.*, the time difference between two
181 estimated origin times).

183 The final catalog contains 714 events (166 foreshocks, 547 aftershocks), which represents
184 ~ 6 -fold the number of events in the initial catalog. To estimate the magnitudes of the
185 newly detected events, we use the average root mean square in the time window containing
186 the S waves over all of the stations and components. Least-square fitting is then used
187 to obtain a linear model that relates the logarithmic of the root mean square of the 23
188 templates and their local magnitudes from the INGV catalog. This model is then used to
189 estimate the magnitude of the newly detected events. A summary of the event occurrences
190 in time together with their magnitudes is shown in Figure 2.

191 [Figure 2]

192 **Waveform-based clustering:** Clustering is widely used in seismology to recognize
193 patterns in spatio-temporal events, which include the identification of foreshock-aftershock
194 sequences and stress evolution in time (*e.g.*, [Kagan and Jackson, 1991](#); [Wehling-Benatelli](#)

195 et al., 2013; Cesca et al., 2014; Ellsworth and Bulut, 2018). Here, we apply waveform simi-
196 larity analysis (Cattaneo et al., 1999) to define groups of events that share similar locations
197 and/or a common rupture mechanism (Kagan and Jackson, 1991; Wehling-Benatelli et al.,
198 2013; Cesca et al., 2014; Ellsworth and Bulut, 2018; Cattaneo et al., 1999). For this, the
199 full normalized waveforms are used, with a 4.5-s time window (starting 0.5 s before the
200 P-wave arrival) that contains both the P phase and the S phase.

201 The waveforms of the 714 detected events recorded at the closest station to the epicenter
202 (Fig. 1, VVLD) are then correlated with each other. The correlation matrix obtained (Fig.
203 3a) is used to estimate the distance (dissimilarity) metric to perform hierarchical clustering.
204 The Ward minimum variance method is used (Ward Jr, 1963) with a distance threshold
205 of 5.5 defined (Supplementary Materials Fig. S1: the largest separation observed from the
206 dendrogram). This waveform similarity analysis highlights five different clusters, as shown
207 in Figure 3b, c. As both the P waves and S waves are used for clustering, the resulting
208 family members should share similarities in position and rupture mechanism (Kagan and
209 Jackson, 1991; Wehling-Benatelli et al., 2013; Cesca et al., 2014; Ellsworth and Bulut, 2018;
210 Cattaneo et al., 1999).

211 **Relocation:** We finally estimate the relative location between the detected events using
212 the double-difference algorithm (HypoDD software; Waldhauser (2001)). The differential
213 times of the P phases and S phases between events from the cross-correlation are estimated,
214 with the retention of only the delays that are associated to correlation coefficients >0.6 .
215 We further limit the delays to 0.2 s. After discarding the event pairs that relate less than
216 3 P-wave and 3 S-wave highly correlated differential times (correlation coefficient, ≥ 0.6),
217 the final number of 29859 pairs are kept and used in the relocation process.

218 For each newly detected event, we assume its initial location as the coordinates of the
219 template that reports the highest correlation coefficient related to that event. In addition,
220 we assume the estimated P-wave and S-wave picks obtained from our template matching
221 analysis as the initial catalog information for the relocation. A velocity model for this region

222 proposed by [Bagh et al. \(2007\)](#) is used in the relocation process (Supplementary Materials
223 Table S3). Following previous studies ([Shelly and Hardebeck, 2019](#)), the inversion is per-
224 formed with stronger weights to the initial information related to the P-wave and S-wave
225 picks from the catalog (*i.e.*, from the template matching analysis), while the differential
226 times from the waveform correlations control the final iterations. In the end, 689 of the
227 714 newly detected events are successfully relocated. The temporal and geometric patterns
228 observed in this earthquake sequence are illustrated in Figures 4 and 5, and are further
229 described in the following section.

230 [Figure 3]

231 Results and discussion

232 The time evolution of the detected events is shown in Figure 2. Of the 714 events, 166 are
233 foreshocks (23%). Together with the temporal evolution, Figure 2a shows the spectrogram
234 and the average spectral energy in a frequency band from 5 Hz to 20 Hz. The oscillation
235 of this energy suggests variable noise levels in the study area, with lower noise during the
236 night (Figure 2, shaded areas, for periods from 18:00 to 06:00). This noise variation is
237 related to anthropogenic activity ([Poli et al., 2020b](#)), and it is also observed for the other
238 five receivers. This noise evolution will probably affect our detection performance. For
239 example, it is not clear if the reduced number of events observed prior to the mainshock is
240 real or is a consequence of the higher noise level (Fig. 2b). We thus avoid discussing any
241 issue related to pre-seismic quiescence here. However, with the geometric and clustering
242 information derived above, we can still characterize some of the properties of the newly
243 detected foreshocks and aftershocks, and gain insight into the physical processes that occur
244 at the different stages of the sequence.

245 The results from the combination of waveform clustering and relocation strategies are
246 summarized in Figures 4 and 5. For each cluster, the coefficient of variation (COV) is also

247 estimated from the recurrence time of the events (Kagan and Jackson, 1991; Schoenball
248 and Ellsworth, 2017). The COV indicates the level of the temporal clustering within each
249 group (*i.e.*, how much the occurrence of future earthquakes depends on the occurrence of the
250 past earthquakes): with COV=1 for random seismicity, and COV>1 for strong temporal
251 clustering. The larger the COV, the more the earthquakes are interacting. Thus, it is
252 important to note that events that happen together with a high COV mean that there is
253 an intrinsically related interaction between them.

254 The temporal and spatial densities of the different clusters identified in this sequence
255 are illustrated in Figure 4, where cluster 1 (green solid lines and dots) is mainly composed
256 of foreshocks (161 of 209 events occurred before the mainshock). The events that form this
257 family show the highest waveform similarity (Fig. 3a). In agreement with this waveform
258 property, cluster 1 has high spatial density, with approximately 90% of its activity (193
259 of the 208 events) located within 0.5 km of the mainshock hypocenter (Figs. 4a and 5a).
260 Cluster 1 also shows the highest temporal clustering (COV=4.8; Fig. 4a).

261 The next two families, as cluster 2 (COV=3.0; Figure 4b, blue solid lines and dots)
262 and cluster 3 (COV=2.9; Figure 4c, magenta solid lines and dots), share similar temporal
263 clustering values, but show differences with respect to their spatial densities. While ap-
264 proximately 90% of the events of cluster 2 are within 0.8 km of the hypocenter (136 of 151
265 events; Fig. 4b), cluster 3 has almost 90% of its activity (187 of 211 events) located over
266 a larger volume, as approximately 1.2 km from the mainshock location (Fig. 4c). Cluster
267 4 (Figure 4d, brown solid lines and dots) is characterized by 90% of its activity within 0.6
268 km of the mainshock hypocenter (53 of 59 shocks; Fig. 4d). The seismicity in this cluster
269 is also characterized by high temporal clustering (COV=4.2). Cluster 5 (COV=2.2; Figure
270 4e, red solid lines and dots) is the least temporally clustered, but with the second highest
271 spatial density (after cluster 1), with 90% of its activity in a region 0.5 km from the main-
272 shock hypocenter (66 of 73 events; Fig. 4e). A general spatial pattern of this sequence is
273 the concentration of events close to the mainshock that occurred prior to it (110 foreshocks

274 within 0.3 km) and the subsequent spread over a region >0.3 km during the aftershocks.

275 Figure 5 illustrates the geometric patterns related to each of the clusters, as defined
276 by the relocation process. A remarkable pattern can be seen in Figure 5a: cluster 1 (*i.e.*,
277 foreshocks) shows an antithetical orientation with respect to the assumed fault plane of
278 the main event (Fig. 5a, map view and cross sections). In contrast, clusters 4 and 5 show
279 nearly parallel orientations with respect to the assumed main fault plane (Fig. 5d, e, cross-
280 sections, respectively). We also observe particular behavior for cluster 5, which is the only
281 cluster where the activity is exclusively to the northeast of the mainshock hypocenter and
282 on the footwall (Fig. 5e, map view and cross-sections). The events in cluster 5 follow an
283 orientation that is parallel to the assumed main fault plane dipping angle (Fig. 5e, cross-
284 section). In turn, cluster 3 has an activity that follows the orientation of the fault plane, but
285 that spreads across the whole volume surrounding the fault plane (Fig. 5c, cross-sections).

286 [Figure 4]

287 [Figure 5]

288 The results of the spatio-temporal evolution for the identified clusters suggest complex
289 evolution of the seismicity. Two fault planes are activated during the sequence, with fore-
290 shocks primarily occurring on the antithetic fault plane (Fig. 5a, cross-section), similarly to
291 part of the foreshock activity that was observed for the L’Aquila normal fault earthquake
292 ([Chiaraluce et al., 2011](#)). Relying only on our observations, it is hard to unravel which
293 mechanism(s) might be responsible for the occurrence of the foreshocks, and thus the driv-
294 ing of the main event. For example, there are no exponential or power-law increments
295 of events seen while approaching the main event ([Papazachos, 1975; Kagan and Knopoff,](#)
296 [1978](#)), which might suggest accelerating aseismic slip ([Dodge et al., 1996; Bouchon et al.,](#)
297 [2011; Tape et al., 2018](#)). Neither are any spatial patterns seen (*e.g.*, migrations) that might
298 suggest the same mechanism, or might alternatively indicate triggering by stress transfer

299 (Dodge et al., 1996; Ellsworth and Bulut, 2018; Yoon et al., 2019). However, we clearly
300 outline the differences between the foreshocks and aftershocks. In particular, the fore-
301 shocks occur in a more temporal clustered manner, and they are closer to the hypocenter
302 of the main event (Fig. 4a). The compact and highly temporal clustered seismicity indi-
303 cates strong event interactions, and favors stress transfer as the mechanism for foreshock
304 occurrence (COV, Schoenball and Ellsworth, 2017).

305 Interestingly, the aftershock clusters also show different spatio-temporal behaviors be-
306 tween each other (Figs. 5b-e, 4b-e). The observed differences might be explained by different
307 physical processes driving the aftershock occurrence. For example, the events in clusters
308 2 and 3 (Fig. 5b,c) spread in a volume around the fault. This spatial pattern is likely
309 to result from stress redistribution, volumetric damage, and relaxation processes after the
310 mainshock (Trugman et al., 2020). In contrast, clusters 4 and 5 follow the orientation of
311 the main fault in a more compact volume around it (Fig. 5d,e), and their activity decays
312 in a rapid manner (Fig. 4). This behavior might suggest that these latter clusters result
313 from stress increments induced by the mainshock afterslip that occurs near the fault plane
314 region in the few hours or days after the main event (Stein and Lisowski, 1983; Shen et al.,
315 1994).

316 As in previous studies (McMahon et al., 2017; Savage et al., 2017; McMahon et al., 2019),
317 we can see that this detailed analysis of seismic data reveals a complex and imbricated
318 earthquake sequence, for which the mainshock initiation is unlikely to result from only the
319 evolution of physical properties (*e.g.*, stress, friction) on the main fault plane. Indeed the
320 sequence begins through an interaction between the antithetic and main faults during the
321 foreshock-mainshock sequences, similar to that observed for other events (Chiaraluce et al.,
322 2011; McMahon et al., 2019). In normal faults, this behavior can be related to preseismic
323 processes in the dilation wedge located in the hanging wall (Doglioni et al., 2011). The
324 complexity of the sequence might also emerge from fluid involvement, which is known to
325 have a significant role in the control of seismicity and its 'style' in the central Apennines

326 (Antonioli et al., 2005; Poli et al., 2020a). The stress perturbations in the antithetic fault
327 might have modified the local pore pressures, with fluid migration into the main fault,
328 which would favor the occurrence of the main event (Doglioni et al., 2011).

329 Conclusion

330 By using a combination of high-resolution detection methods, precise relocation (*e.g.*, Gib-
331 bons and Ringdal, 2006; Waldhauser, 2001) and waveform clustering, we have unveiled
332 the complexity of the sequences associated with the 2019 (M_w 4.4) Balsorano earthquake.
333 We detect 714 events that comprise this sequence. These events are classified into five
334 different seismic clusters. The differences between these clusters are highlighted by their
335 distinct spatio-temporal properties that are unveiled by the waveform-based clustering anal-
336 ysis (Kagan and Jackson, 1991; Wehling-Benatelli et al., 2013; Cesca et al., 2014; Ellsworth
337 and Bulut, 2018), and by their relative source locations (Waldhauser, 2001).

338 Our results highlight different behaviors between foreshocks and aftershocks. For exam-
339 ple, foreshocks occur in a compact region near the mainshock hypocenter, and show high
340 temporal clustering (Fig. 4a). The lack of repeating events (*i.e.*, highly correlated events
341 with correlation coefficient >0.9), strong temporal clustering, and inter-event proximity
342 might indicate that stress transfer triggering has the main role in driving the occurrence
343 of the foreshocks (Dodge et al., 1996). Nevertheless, there are no observations that can
344 exclude aseismic slip. The foreshock activity mainly take place in an antithetic fault (Fig.
345 5a), which suggests that the initiation processes do not only occur on one fault plane, but
346 involve larger volumes (Savage et al., 2017). This precursory antithetic activation has been
347 observed in other normal fault events (Chiaraluce et al., 2011) and it can be expected in
348 some gravity-driven normal fault models (Doglioni et al., 2011).

349 Furthermore, our analysis shows diversity for the aftershocks behavior. Indeed, four
350 different clusters comprise the aftershock sequences. Two of these four are spread in a

volume around the main fault (Fig. 5b,c), and might result from stress redistribution after the mainshock (*e.g.*, caused by volumetric damage and the relaxation processes; Trugman et al. (2020)). Given the rapid temporal decay of their activity and their compactness and spatial orientation, the remaining two clusters appear to be driven by rapid stress increments induced by the mainshock and afterslip that occur near the fault plane in the few days after the mainshock (Stein and Lisowski, 1983; Shen et al., 1994).

In summary, this study of foreshocks and aftershocks highlights that simple preparation models with evolution of stress and friction on a single fault plane are not suited to precisely explain the evolution of the seismicity we observe here for a real fault. A relatively large volume appears to be involved in the earthquake initiation, over a short time scale (\sim 1 day). We further highlight how the full range of aftershocks is likely to be an ensemble average view of different processes, which will include afterslip, volumetric damage, and relaxation. Continuing to provide detailed information about foreshocks and their relationships to the mainshock and aftershocks also for relatively small events can help us to develop new and more realistic models that can provide better fitting of seismological observations and shed new light on the initiation of earthquakes in real faults.

367 Data and resources

The continuous seismic data used in this study are available at the Istituto Nazionale di Geofisica e Vulcanologia (INGV) seismological data center (http://cnt.rm.ingv.it/webservices_and_software/; last accessed, March 2020) and were downloaded using obspyDMT (<https://github.com/kasra-hosseini/obspyDMT>, Hosseini and Sigloch (2017)). The fast matched filter (Beaucé et al., 2017) used in this study can be found at https://github.com/beridel/fast_matched_filter. Some plots were made using the Generic Mapping Tools version 4.5.14 (www.soest.hawaii.edu/gmt; Wessel and Smith (1998)). The event clustering was performed using Scikit-learn (<https://scikit-learn.org/stable/>; Pedregosa et al. (2011))

³⁷⁶ Acknowledgments

³⁷⁷ This research received funding from the European Research Council (ERC) under the Euro-
³⁷⁸ pean Union Horizon 2020 Research and Innovation Programme (grant agreement 802777-
³⁷⁹ MONIFAULTS). Computations were performed using the Univerty of Grenoble Alpes
³⁸⁰ (UGA) High-Performance Computing infrastructures CIMENT
³⁸¹ (<https://ciment.univ-grenoble-alpes.fr>).

³⁸² References

- ³⁸³ Abercrombie, R. E. and Mori, J. (1996). Occurrence patterns of foreshocks to large earth-
³⁸⁴ quakes in the western united states. *Nature*, 381(6580):303–307.
- ³⁸⁵ Antonioli, A., Piccinini, D., Chiaraluce, L., and Cocco, M. (2005). Fluid flow and seis-
³⁸⁶ micity pattern: Evidence from the 1997 umbria-marche (central italy) seismic sequence.
³⁸⁷ *Geophysical Research Letters*, 32(10).
- ³⁸⁸ Bagh, S., Chiaraluce, L., De Gori, P., Moretti, M., Govoni, A., Chiarabba, C., Di Bar-
³⁸⁹ tolomeo, P., and Romanelli, M. (2007). Background seismicity in the central apennines
³⁹⁰ of italy: The abruzzo region case study. *Tectonophysics*, 444(1-4):80–92.
- ³⁹¹ Beaucé, E., Frank, W. B., and Romanenko, A. (2017). Fast matched filter (fmf): An
³⁹² efficient seismic matched-filter search for both cpu and gpu architectures. *Seismological*
³⁹³ *Research Letters*, 89(1):165.
- ³⁹⁴ Bouchon, M., Durand, V., Marsan, D., Karabulut, H., and Schmittbuhl, J. (2013). The long
³⁹⁵ precursory phase of most large interplate earthquakes. *Nature geoscience*, 6(4):299–302.
- ³⁹⁶ Bouchon, M., Karabulut, H., Aktar, M., Özalaybey, S., Schmittbuhl, J., and Bouin, M.-P.
³⁹⁷ (2011). Extended nucleation of the 1999 mw 7.6 izmit earthquake. *science*, 331(6019):877–
³⁹⁸ 880.

- 399 Brune, J. N. (1979). Implications of earthquake triggering and rupture propagation for
400 earthquake prediction based on premonitory phenomena. *Journal of Geophysical Re-*
401 *search: Solid Earth*, 84(B5):2195–2198.
- 402 Cattaneo, M., Augliera, P., Spallarossa, D., and Lanza, V. (1999). A waveform similarity
403 approach to investigate seismicity patterns. *Natural hazards*, 19(2-3):123–138.
- 404 Cesca, S., Sen, A. T., and Dahm, T. (2014). Seismicity monitoring by cluster analysis of
405 moment tensors. *Geophysical Journal International*, 196(3):1813–1826.
- 406 Chen, X. and Shearer, P. M. (2013). California foreshock sequences suggest aseismic trig-
407 gering process. *Geophysical Research Letters*, 40(11):2602–2607.
- 408 Chiaraluce, L., Valoroso, L., Piccinini, D., Di Stefano, R., and De Gori, P. (2011). The
409 anatomy of the 2009 l'aquila normal fault system (central italy) imaged by high resolu-
410 tion foreshock and aftershock locations. *Journal of Geophysical Research: Solid Earth*,
411 116(B12).
- 412 D'agostino, N., Giuliani, R., Mattone, M., and Bonci, L. (2001). Active crustal extension in
413 the central apennines (italy) inferred from gps measurements in the interval 1994–1999.
414 *Geophysical Research Letters*, 28(10):2121–2124.
- 415 De Santis, A., Marchetti, D., Pavón-Carrasco, F. J., Cianchini, G., Perrone, L., Abbattista,
416 C., Alfonsi, L., Amoruso, L., Campuzano, S. A., Carbone, M., et al. (2019). Precursory
417 worldwide signatures of earthquake occurrences on swarm satellite data. *Scientific reports*,
418 9(1):1–13.
- 419 Dieterich, J. (1994). A constitutive law for rate of earthquake production and its application
420 to earthquake clustering. *Journal of Geophysical Research: Solid Earth*, 99(B2):2601–
421 2618.

- 422 Dieterich, J. H. (1992). Earthquake nucleation on faults with rate-and state-dependent
423 strength. *Tectonophysics*, 211(1-4):115–134.
- 424 Dodge, D. A., Beroza, G. C., and Ellsworth, W. (1996). Detailed observations of califor-
425 nia foreshock sequences: Implications for the earthquake initiation process. *Journal of*
426 *Geophysical Research: Solid Earth*, 101(B10):22371–22392.
- 427 Doglioni, C., Barba, S., Carminati, E., and Riguzzi, F. (2011). Role of the brittle–ductile
428 transition on fault activation. *Physics of the Earth and Planetary Interiors*, 184(3-4):160–
429 171.
- 430 Dublanchet, P. (2018). The dynamics of earthquake precursors controlled by effective fric-
431 tion. *Geophysical Journal International*, 212(2):853–871.
- 432 Eftaxias, K., Kopanas, J., Bogris, N., KAPIRIS, P., ANTONOPOULOS, G., and VAROT-
433 SOS, P. (2000). Detection of electromagnetic earthquake precursory signals in greece.
434 *Proceedings of the Japan Academy, Series B*, 76(4):45–50.
- 435 Ellsworth, W. L. and Beroza, G. C. (1995). Seismic evidence for an earthquake nucleation
436 phase. *Science*, 268(5212):851–855.
- 437 Ellsworth, W. L. and Bulut, F. (2018). Nucleation of the 1999 izmit earthquake by a
438 triggered cascade of foreshocks. *Nature Geoscience*, 11(7):531–535.
- 439 Felzer, K. R., Abercrombie, R. E., and Ekstrom, G. (2004). A common origin for af-
440 tershocks, foreshocks, and multiplets. *Bulletin of the Seismological Society of America*,
441 94(1):88–98.
- 442 Gibbons, S. J. and Ringdal, F. (2006). The detection of low magnitude seismic events using
443 array-based waveform correlation. *Geophysical Journal International*, 165(1):149–166.

- 444 Goebel, T., Becker, T., Schorlemmer, D., Stanchits, S., Sammis, C., Rybacki, E., and
445 Dresen, G. (2012). Identifying fault heterogeneity through mapping spatial anomalies in
446 acoustic emission statistics. *Journal of Geophysical Research: Solid Earth*, 117(B3).
- 447 Hosseini, K. and Sigloch, K. (2017). Obspydmt: a python toolbox for retrieving and pro-
448 cessing large seismological data sets. *Solid Earth*, (5):1047–1070.
- 449 Hunstad, I. and England, P. (1999). An upper bound on the rate of strain in the central
450 apennines, italy, from triangulation measurements between 1869 and 1963. *Earth and*
451 *Planetary Science Letters*, 169(3-4):261–267.
- 452 Jones, L. M. and Molnar, P. (1979). Some characteristics of foreshocks and their pos-
453 sible relationship to earthquake prediction and premonitory slip on faults. *Journal of*
454 *Geophysical Research: Solid Earth*, 84(B7):3596–3608.
- 455 Jones, L. M. (1985). Foreshocks and time-dependent earthquake hazard assessment in
456 southern california. *Bulletin of the Seismological Society of America*, 75(6):1669–1679.
- 457 Kagan, Y. and Jackson, D. D. (1991). Long-term earthquake clustering. *Geophysical Journal*
458 *International*, 104(1):117–133.
- 459 Kagan, Y. and Knopoff, L. (1978). Statistical study of the occurrence of shallow earth-
460 quakes. *Geophysical Journal International*, 55(1):67–86.
- 461 Kato, A., Obara, K., Igarashi, T., Tsuruoka, H., Nakagawa, S., and Hirata, N. (2012).
462 Propagation of slow slip leading up to the 2011 mw 9.0 tohoku-oki earthquake. *Science*,
463 335(6069):705–708.
- 464 Liu, Y. and Rice, J. R. (2005). Aseismic slip transients emerge spontaneously in three-
465 dimensional rate and state modeling of subduction earthquake sequences. *Journal of*
466 *Geophysical Research: Solid Earth*, 110(B8).

- 467 Malin, P. E., Bohnhoff, M., Blümle, F., Dresen, G., Martínez-Garzón, P., Nurlu, M., Ceken,
468 U., Kadirioglu, F. T., Kartal, R. F., Kilic, T., et al. (2018). Microearthquakes preceding
469 a m4. 2 earthquake offshore istanbul. *Scientific reports*, 8(1):1–11.
- 470 Marone, C. (1998). The effect of loading rate on static friction and the rate of fault healing
471 during the earthquake cycle. *Nature*, 391(6662):69–72.
- 472 McLaskey, G. C. (2019). Earthquake initiation from laboratory observations and implica-
473 tions for foreshocks. *Journal of Geophysical Research: Solid Earth*.
- 474 McMahon, N. D., Aster, R. C., Yeck, W. L., McNamara, D. E., and Benz, H. M. (2017).
475 Spatiotemporal evolution of the 2011 prague, oklahoma, aftershock sequence revealed
476 using subspace detection and relocation. *Geophysical Research Letters*, 44(14):7149–7158.
- 477 McMahon, N. D., Yeck, W. L., Stickney, M. C., Aster, R. C., Martens, H. R., and Benz,
478 H. M. (2019). Spatiotemporal analysis of the foreshock–mainshock–aftershock sequence
479 of the 6 july 2017 m w 5.8 lincoln, montana, earthquake. *Seismological Research Letters*,
480 90(1):131–139.
- 481 Mignan, A. (2014). The debate on the prognostic value of earthquake foreshocks: A meta-
482 analysis. *Scientific reports*, 4:4099.
- 483 Mogi, K. (1963). Some discussions on aftershocks, foreshocks and earthquake swarms:
484 the fracture of a semi-infinite body caused by an inner stress origin and its relation to
485 the earthquake phenomena (third paper). *Bulletin of the Earthquake Research Institute,*
486 *University of Tokyo*, 41(3):615–658.
- 487 Molchanov, O., Hayakawa, M., Oudoh, T., and Kawai, E. (1998). Precursory effects in the
488 subionospheric vlf signals for the kobe earthquake. *Physics of the Earth and Planetary*
489 *Interiors*, 105(3-4):239–248.

- 490 Papazachos, B. (1975). Foreshocks and earthquake prediction. *Tectonophysics*, 28(4):213–
491 226.
- 492 Pedregosa, F., Varoquaux, G., Gramfort, A., Michel, V., Thirion, B., Grisel, O., Blondel,
493 M., Prettenhofer, P., Weiss, R., Dubourg, V., Vanderplas, J., Passos, A., Cournapeau,
494 D., Brucher, M., Perrot, M., and Duchesnay, E. (2011). Scikit-learn: Machine learning
495 in Python. *Journal of Machine Learning Research*, 12:2825–2830.
- 496 Poli, P., Marguin, V., Wang, Q., Dagostino, N., and Johnson, P. (2020a). Seasonal and co-
497 seismic velocity variation in the region of laquila from single station measurements and
498 implications for crustal rheology. *Journal of Geophysical Research: Solid Earth*, page
499 e2019JB019316.
- 500 Poli, P., Soaga, J., Molinari, I., Cascone, V., and Boschi, L. (2020b). The 2020 coronavirus
501 lockdown and seismic monitoring of anthropic activities in northern italy. *Sci Rep*, 10:–.
- 502 Reasenberg, P. A. (1999). Foreshock occurrence before large earthquakes. *Journal of*
503 *Geophysical Research: Solid Earth*, 104(B3):4755–4768.
- 504 Renard, F., McBeck, J., Kandula, N., Cordonnier, B., Meakin, P., and Ben-Zion, Y. (2019).
505 Volumetric and shear processes in crystalline rock approaching faulting. *Proceedings of*
506 *the National Academy of Sciences*, 116(33):16234–16239.
- 507 Rikitake, T. (1975). Earthquake precursors. *Bulletin of the Seismological Society of Amer-*
508 *ica*, 65(5):1133–1162.
- 509 Roberts, G. P. and Michetti, A. M. (2004). Spatial and temporal variations in growth rates
510 along active normal fault systems: an example from the lazio–abruzzo apennines, central
511 italy. *Journal of Structural Geology*, 26(2):339–376.
- 512 Rubin, A. M. and Ampuero, J.-P. (2005). Earthquake nucleation on (aging) rate and state
513 faults. *Journal of Geophysical Research: Solid Earth*, 110(B11).

- 514 Ruiz, S., Aden-Antoniow, F., Baez, J., Otarola, C., Potin, B., del Campo, F., Poli, P.,
515 Flores, C., Satriano, C., Leyton, F., et al. (2017). Nucleation phase and dynamic inversion
516 of the mw 6.9 valparaíso 2017 earthquake in central chile. *Geophysical Research Letters*,
517 44(20):10–290.
- 518 Ruiz, S., Metois, M., Fuenzalida, A., Ruiz, J., Leyton, F., Grandin, R., Vigny, C.,
519 Madariaga, R., and Campos, J. (2014a). Intense foreshocks and a slow slip event preceded
520 the 2014 iquique mw 8.1 earthquake. *Science*, 345(6201):1165–1169.
- 521 Ruiz, S., Metois, M., Fuenzalida, A., Ruiz, J., Leyton, F., Grandin, R., Vigny, C.,
522 Madariaga, R., and Campos, J. (2014b). Intense foreshocks and a slow slip event preceded
523 the 2014 iquique mw 8.1 earthquake. *Science*, 345(6201):1165–1169.
- 524 Savage, H. M., Keranen, K. M., P. Schaff, D., and Dieck, C. (2017). Possible precursory
525 signals in damage zone foreshocks. *Geophysical Research Letters*, 44(11):5411–5417.
- 526 Schoenball, M. and Ellsworth, W. L. (2017). A systematic assessment of the spatiotemporal
527 evolution of fault activation through induced seismicity in oklahoma and southern kansas.
528 *Journal of Geophysical Research: Solid Earth*, 122(12):10–189.
- 529 Schurr, B., Asch, G., Hainzl, S., Bedford, J., Hoechner, A., Palo, M., Wang, R., Moreno,
530 M., Bartsch, M., Zhang, Y., et al. (2014). Gradual unlocking of plate boundary controlled
531 initiation of the 2014 iquique earthquake. *Nature*, 512(7514):299–302.
- 532 Shelly, D. R., Beroza, G. C., and Ide, S. (2007). Complex evolution of transient slip de-
533 rived from precise tremor locations in western shikoku, japan. *Geochemistry, Geophysics,
534 Geosystems*, 8(10).
- 535 Shelly, D. R. and Hardebeck, J. L. (2019). Illuminating faulting complexity of the 2017
536 yellowstone maple creek earthquake swarm. *Geophysical Research Letters*, 46(5):2544–
537 2552.

- 538 Shen, Z.-K., Jackson, D. D., Feng, Y., Cline, M., Kim, M., Fang, P., and Bock, Y. (1994).
539 Postseismic deformation following the landers earthquake, california, 28 june 1992. *Bul-*
540 *letin of the Seismological Society of America*, 84(3):780–791.
- 541 Singh, R. P., Mehdi, W., Gautam, R., Senthil Kumar, J., Zlotnicki, J., and Kafatos, M.
542 (2010). Precursory signals using satellite and ground data associated with the wenchuan
543 earthquake of 12 may 2008. *International Journal of Remote Sensing*, 31(13):3341–3354.
- 544 Stein, R. S. and Lisowski, M. (1983). The 1979 homestead valley earthquake sequence,
545 california: Control of aftershocks and postseismic deformation. *Journal of Geophysical*
546 *Research: Solid Earth*, 88(B8):6477–6490.
- 547 Tape, C., Holtkamp, S., Silwal, V., Hawthorne, J., Kaneko, Y., Ampuero, J. P., Ji, C.,
548 Ruppert, N., Smith, K., and West, M. E. (2018). Earthquake nucleation and fault slip
549 complexity in the lower crust of central alaska. *Nature Geoscience*, 11(7):536–541.
- 550 Tramutoli, V., Corrado, R., Filizzola, C., Genzano, N., Lisi, M., and Pergola, N. (2015).
551 From visual comparison to robust satellite techniques: 30 years of thermal infrared satel-
552 lite data analyses for the study of earthquake preparation phases. *Bollettino di Geofisica*
553 *Teorica ed Applicata*, 56(2).
- 554 Trugman, D. T., Ross, Z. E., and Johnson, P. A. (2020). Imaging stress and fault-
555 ing complexity through earthquake waveform similarity. *Geophysical Research Letters*,
556 47(1):e2019GL085888.
- 557 Virk, H. and Walia, V. (2001). Helium/radon precursory signals of chamoli earthquake,
558 india. *Radiation measurements*, 34(1-6):379–384.
- 559 Waldhauser, F. (2001). hypodda program to compute double-difference hypocenter loca-
560 tions (hypodd version 1.0-03/2001). *US Geol. Surv. Open File Rep.*, 01, 113.

- 561 Ward Jr, J. H. (1963). Hierarchical grouping to optimize an objective function. *Journal of*
562 *the American statistical association*, 58(301):236–244.
- 563 Wehling-Benatelli, S., Becker, D., Bischoff, M., Friederich, W., and Meier, T. (2013). In-
564 dications for different types of brittle failure due to active coal mining using waveform
565 similarities of induced seismic events. *Solid Earth*, 4(2).
- 566 Wessel, P. and Smith, W. H. (1998). New, improved version of generic mapping tools
567 released. *Eos, Transactions American Geophysical Union*, 79(47):579–579.
- 568 Westaway, R. (1992). Seismic moment summation for historical earthquakes in italy: tec-
569 tonic implications. *Journal of Geophysical Research: Solid Earth*, 97(B11):15437–15464.
- 570 Yoon, C. E., Yoshimitsu, N., Ellsworth, W. L., and Beroza, G. C. (2019). Foreshocks and
571 mainshock nucleation of the 1999 m w 7.1 hector mine, california, earthquake. *Journal*
572 *of Geophysical Research: Solid Earth*, 124(2):1569–1582.
- 573 Zang, A., Christian Wagner, F., Stanchits, S., Dresen, G., Andresen, R., and Haidekker,
574 M. A. (1998). Source analysis of acoustic emissions in aue granite cores under symmetric
575 and asymmetric compressive loads. *Geophysical Journal International*, 135(3):1113–1130.

⁵⁷⁶ **Figure Captions**

Figure 1. Regional map of the study area. The yellow square inside the small map inset on the left corresponds to the central region of Italy represented in the larger topographic map. The small map inset on the right represents magnification of the black dashed area around the epicentral location (red star). The color code used in the map view on the right represents the estimated depth of the foreshock and aftershock activity (estimated in this study: 714 events). The yellow circle represents Balsorano city, and the white triangles represent the stations used in this study. The dashed lines in the right inset map represent the directions A-A' (along strike) and B-B' (normal to the strike) illustrated in the cross sections of Figure 5. The solid – line represents the surface scarp of Liri fault (CITE).

Figure 2. (a) Spectrogram on VVLD.HHZ. The white line is the median of the energy in the frequency band between 5 Hz and 20 Hz calculated within a 1-h sliding window. Notice the diurnal energy variation. (b) Blue, cumulative events for the same time period of the experiment; orange, recurrence time for the newly detected events. (c) Estimated magnitudes for the newly detected events. A gap in the continuous data at this receiver location is seen for the night of November 8 to 9, 2019. In all pannels, day and night periods are represented by shaded (18:00 to 6:00) and unshaded (6:00 to 18:00) regions.

Figure 3. Illustration of the waveform-based hierarchical clustering output. (a) Pairwise correlation coefficients between the waveforms for the vertical component of station VVLD (Fig. 1) of the 714 detected events. This matrix is used to perform the hierarchical clustering. (b) Cumulative events combined with the results from the hierarchical clustering, according to the color code in the legend. (c) Characteristic normalized waveforms (vertical component) of the five different clusters revealed in the earthquake sequence. These traces

are obtained after stacking all of the individually normalized waveforms belonging to each cluster.

Figure 4. Spatio-temporal evolution of the earthquake sequences with respect to the mainshock origin time and hypocenter. Left column: Temporal density (number of events per hour). The coefficients of variation (COV) from the recurrence times are indicated for each cluster. Center column: Distance in time and space from each event of the sequence with respect to the mainshock location and origin time. The dashed grey line on the left and center column represents the mainshock origin time. Right column: Spatial density (concentration of events per 0.1 km). Dashed black line, where 90% of the seismic activity is concentrated. (a)-(e) Each of the five clusters progressively ordered. The same color code from Figure 3 is used.

Figure 5. Map view (left column), and cross-sections along the strike (middle column) and normal-strike (right column) directions for each of the five clusters identified in the sequence (as indicated). All of the locations are relative to the mainshock hypocenter (41.7746°N 13.6066°E ; 13.94 km depth, black star). In all of the panels, the same color code is used as in Figures 3 and 4 to represent each different cluster. The solid black line represents a fault plane of 1 km^2 with the geometry of the second nodal plane (Supplementary Materials Table S1). The dashed blue line represents the assumed auxiliary nodal plane. The directions A-A' (along strike) and B-B' (normal to the strike) are the same as in Figure 1. Each cluster is represented by a correponding label a) Cluster 1 , b) Cluster 2, c) Cluster 3, d) Cluster 4 and e) Cluster 5. In each panel, the open circles represent the location of the templates belonging to each cluster.

⁵⁷⁷ **Figures**

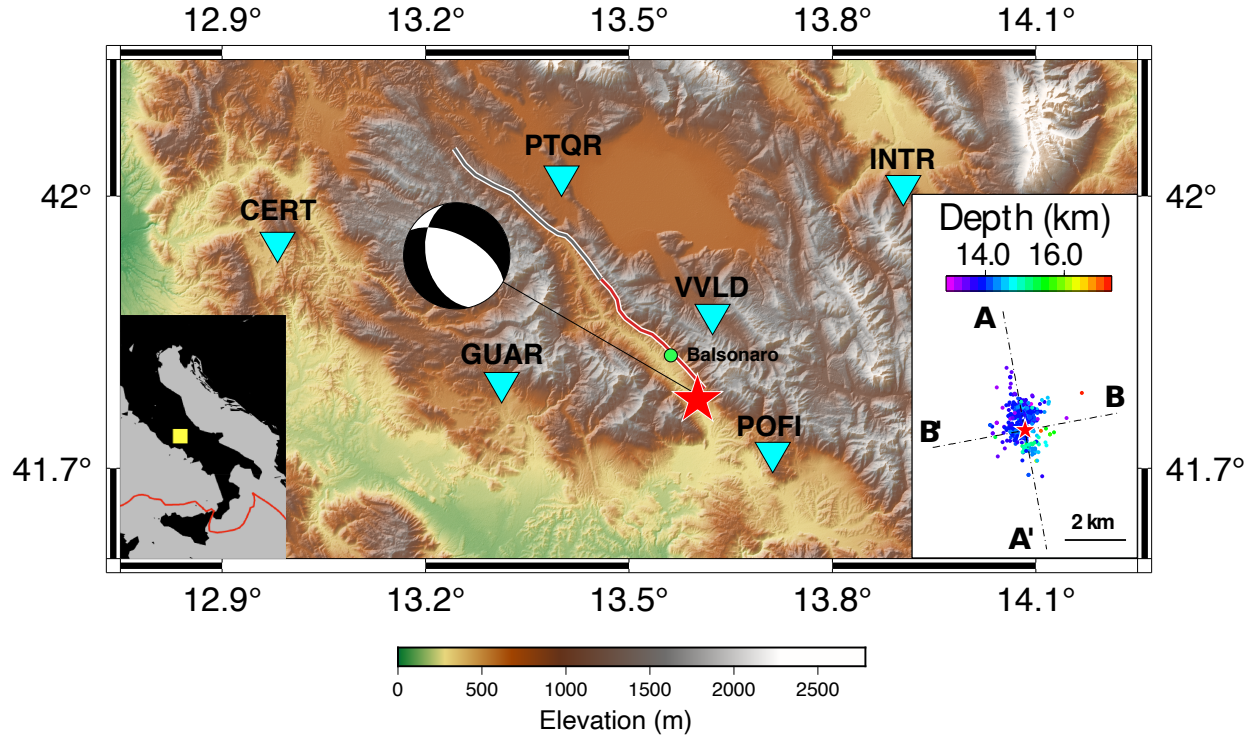


Figure 1: Regional map of the study area. The yellow square inside the small map inset on the left corresponds to the central region of Italy represented in the larger topographic map. The small map inset on the right represents magnification of the black dashed area around the epicentral location (red star). The color code used in the map view on the right represents the estimated depth of the foreshock and aftershock activity (estimated in this study: 714 events). The yellow circle represents Balsorano city, and the white triangles represent the stations used in this study. The dashed lines in the right inset map represent the directions A-A' (along strike) and B-B' (normal to the strike) illustrated in the cross sections of Figure 5. The solid – line represents the surface scarp of Liri fault (CITE).

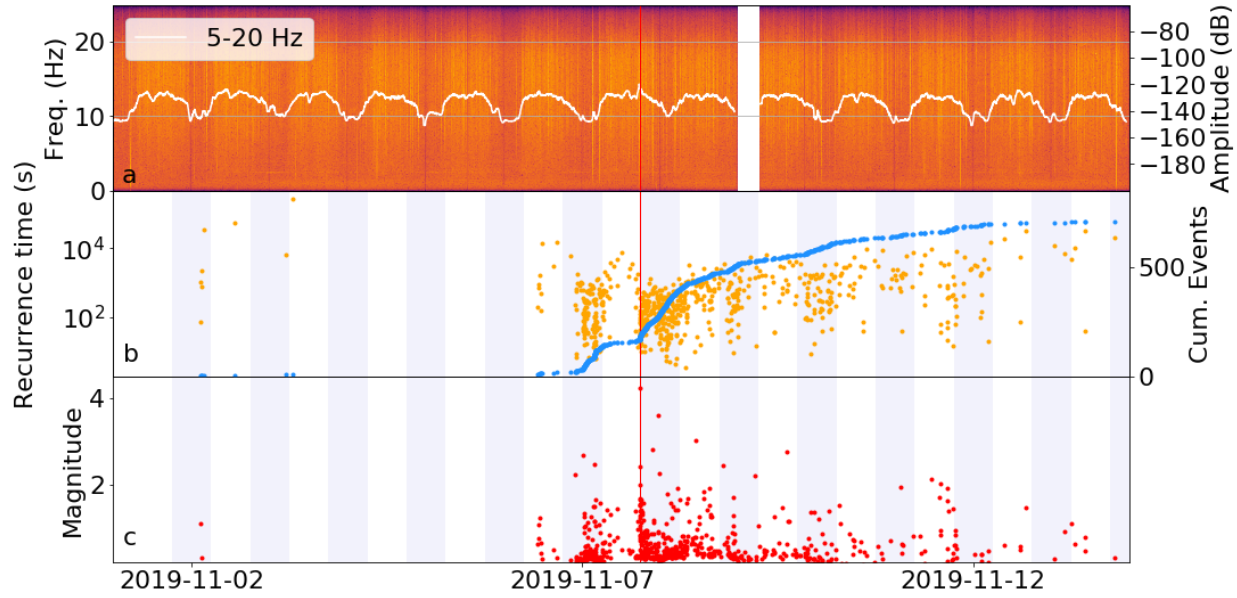


Figure 2: (a) Spectrogram on VVLD.HHZ. The white line is the median of the energy in the frequency band between 5 Hz and 20 Hz calculated within a 1-h sliding window. Notice the diurnal energy variation. (b) Blue, cumulative events for the same time period of the experiment; orange, recurrence time for the newly detected events. (c) Estimated magnitudes for the newly detected events. A gap in the continuous data at this receiver location is seen for the night of November 8 to 9, 2019. In all panels, day and night periods are represented by shaded (18:00 to 6:00) and unshaded (6:00 to 18:00) regions.

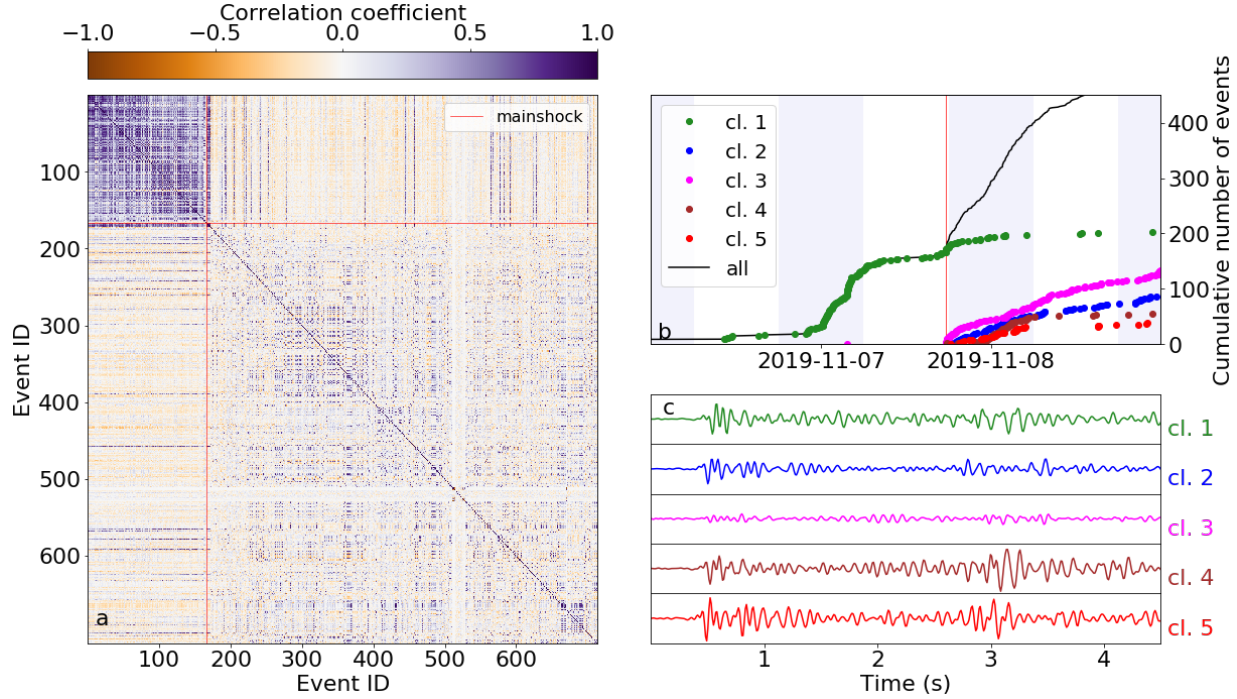


Figure 3: Illustration of the waveform-based hierarchical clustering output. (a) Pairwise correlation coefficients between the waveforms for the vertical component of station VVLD (Fig. 1) of the 714 detected events. This matrix is used to perform the hierarchical clustering. (b) Cumulative events combined with the results from the hierarchical clustering, according to the color code in the legend. (c) Characteristic normalized waveforms (vertical component) of the five different clusters revealed in the earthquake sequence. These traces are obtained after stacking all of the individually normalized waveforms belonging to each cluster.

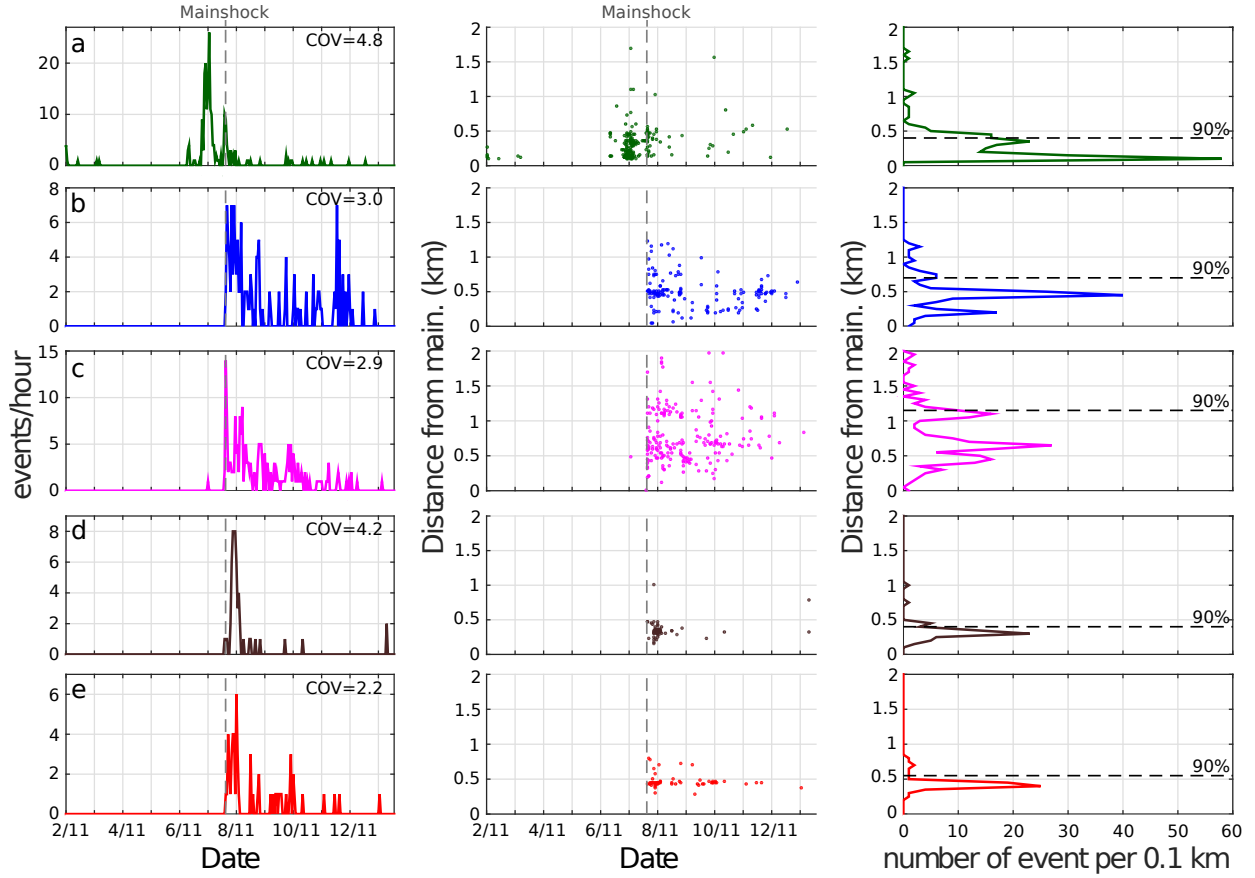


Figure 4: Spatio-temporal evolution of the earthquake sequences with respect to the mainshock origin time and hypocenter. Left column: Temporal density (number of events per hour). The coefficients of variation (COV) from the recurrence times are indicated for each cluster. Center column: Distance in time and space from each event of the sequence with respect to the mainshock location and origin time. The dashed grey line on the left and center column represents the mainshock origin time. Right column: Spatial density (concentration of events per 0.1 km). Dashed black line, where 90% of the seismic activity is concentrated. (a)-(e) Each of the five clusters progressively ordered. The same color code from Figure 3 is used.

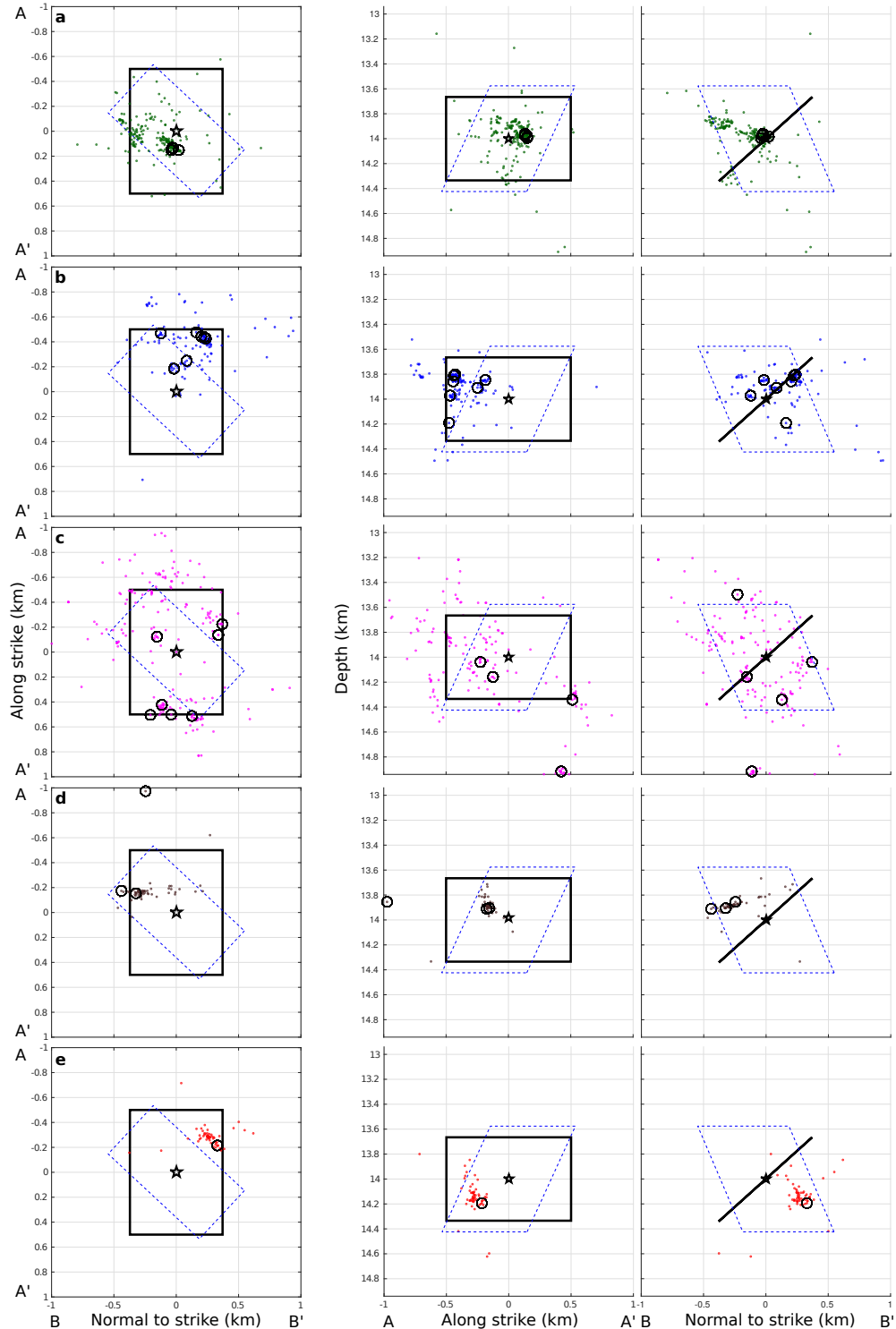


Figure 5: Map view (left column), and cross-sections along the strike (middle column) and normal-strike (right column) directions for each of the five clusters identified in the sequence (as indicated). All of the locations are relative to the mainshock hypocenter (41.7746°N ; 13.6066°E ; 13.94 km depth, black star). In all of the panels, the same color code is used as in Figures 3 and 4 to represent each different cluster. The solid black line represents a fault plane of 1 km^2 with the geometry of the second nodal plane (Supplementary Materials Table 32)